EBM

Experimental Biology and Medicine

The Potential of Dual Camera Systems for Multimodal Imaging of Cardiac Electrophysiology and Metabolism

Mark R. Holcomb, Marcella C. Woods, Ilija Uzelac, John P. Wikswo, Jonathan M. Gilligan and Veniamin Y. Sidorov

The Potential of Dual Camera Systems for Multimodal Imaging of Cardiac Electrophysiology and Metabolism

MARK R. HOLCOMB,[*,1] **MARCELLA C. WOODS,**[†] **ILIJA UZELAC,**[*] **JOHN P. WIKSWO,**[*,†,‡,§]
JONATHAN M. GILLIGAN,[*] **AND VENIAMIN Y. SIDOROV**[†,§,2]

**Department of Physics and Astronomy, Vanderbilt University, Nashville, Tennessee 37235-1807;
†Department of Biomedical Engineering, Vanderbilt University, Nashville, Tennessee 37235-1631;
‡Department of Molecular Physiology and Biophysics, Vanderbilt University, Nashville, Tennessee 37235-0615; and §Vanderbilt Institute for Integrative Biosystems Research and Education, Vanderbilt University, Nashville, Tennessee 37235-1807*

Fluorescence imaging has become a common modality in cardiac electrodynamics. A single fluorescent parameter is typically measured. Given the growing emphasis on simultaneous imaging of more than one cardiac variable, we present an analysis of the potential of dual camera imaging, using as an example our straightforward dual camera system that allows simultaneous measurement of two dynamic quantities from the same region of the heart. The advantages of our system over others include an optional software camera calibration routine that eliminates the need for precise camera alignment. The system allows for rapid setup, dichroic image separation, dual-rate imaging, and high spatial resolution, and it is generally applicable to any two-camera measurement. This type of imaging system offers the potential for recording simultaneously not only transmembrane potential and intracellular calcium, two frequently measured quantities, but also other signals more directly related to myocardial metabolism, such as $[K^+]_e$, NADH, and reactive oxygen species, leading to the possibility of correlative multimodal cardiac imaging. We provide a compilation of dye and camera information critical to the design of dual camera systems and experiments. Exp Biol Med 234:1355–1373, 2009

Introduction

Fluorescence imaging has become the primary modality for studying the electrodynamics of isolated hearts. Typically a single dye is used, and by monitoring the intensity of the fluorescence, a dynamic quantity can be observed. Frequently measured parameters in cardiac electrophysiology are transmembrane potential (V_m) and intracellular calcium concentration ($[Ca^{2+}]_i$). Ideally, both are viewed simultaneously (1), and there is a growing number of published reports of simultaneous V_m and $[Ca^{2+}]_i$ in cardiac tissue using different imaging methods. Dual photodiode arrays have been developed, but these systems require precise alignment because of the small number of pixels (2–4). As an example of the growing number of V_m–$[Ca^{2+}]_i$ studies, Omichi *et al.* (5) reported a study on whole hearts that examined V_m and $[Ca^{2+}]_i$ dynamics during ventricular fibrillation. They employed two cameras with appropriate filters placed side-by-side that were manually aligned to view approximately the same area of the heart. A more recent study by Hwang *et al.* (6) examined simultaneous V_m and $[Ca^{2+}]_i$ dynamics during defibrillation in rabbit hearts. They used two CCD cameras with different perspectives and implanted four cactus needles into the heart as registration markers for use in a software program to match the V_m and $[Ca^{2+}]_i$ pixels to the same location. This methodology, which cannot provide the single-optical path of our approach, also introduces potential error in the data, as heterogeneities inserted in tissue produce shock-induced

[1] Current address: Department of Physics, Davidson College, Davidson, North Carolina 28035.

[2] To whom correspondence should be addressed at Vanderbilt University, Department of Biomedical Engineering, 2301 Vanderbilt Place, Nashville, TN 37235. E-mail: v.sidorov@vanderbilt.edu

changes in polarization (7, 8). Hoeker *et al*. (9) describe a multimodal optical mapping system that uses a dichroic mirror to perform dual calcium–voltage (3) and ratiometric calcium optical mapping (10) in the same cardiac preparation and used it to study an animal model of heart failure. Chuck *et al*. (11) reported on V_m and $[Ca^{2+}]_i$ activity in embryonic hearts using two cameras interfaced with a fluorescence microscope. The system we have developed addresses a different set of technical issues than those that occur with microscope imaging of planar cultures, small hearts, or restricted epicardial imaging at very high magnification.

The challenge of controlling and synchronizing multiple cameras can be addressed using individual frame grabbers and custom software (12, 13), or with a commercial camera controller designed to support two cameras (for example, the MiCAM02 Dual Camera System, Scimedia USA Ltd, Irvine, CA). The latter approach has been used recently to image V_m and $[Ca^{2+}]_i$ in the *in vivo* mouse brain (14), although no details are provided regarding the dual camera optical configuration. While most recent reports use multiple cameras, it is also possible to use mirrors to project two or more separate images onto the focal plane of a single camera, as was done for monochrome panoramic imaging of the epicardial V_m distribution of a rabbit heart (13), or for multicolor imaging with a microscope (Dual-View and Quad-View, MAG Biosystems, Tucson, AZ).

In this paper, we describe a very straightforward dual CCD camera system which permits simultaneous measurement of two dynamic quantities from the same region. Our system is unique for a number of reasons. It is designed for rapid setup and has high spatial resolution over a large field of view. It utilizes dichroic image separation so that image acquisition is through a single optical path which maximizes light detection efficiency, eliminates parallax, and simplifies alignment of the images. The system can also be used to provide two separate image magnifications or camera frame rates. The computer control system supports configuration files that readily allow changes in camera parameters or the hardware setup. In the Results section we present multiple demonstrations of the utility of this dual camera system. We also analyze various issues regarding selection of dyes and illumination wavelengths for dual imaging as applied to cardiac metabolic measurements. The flexibility and simplicity of a dual camera system should enable a broader application of multimodal cardiac imaging.

Methods

Dual Camera Setup. Our dual camera system, in the configuration for simultaneous V_m and $[Ca^{2+}]_i$ imaging, is shown in Figure 1A. The first optical element is a dichroic mirror (635 DCLP, Omega Optical), oriented at 45° with respect to both cameras, that reflects the $[Ca^{2+}]_i$ signal and transmits the V_m signal. The V_m camera uses a 710 nm long pass filter (25 mm round 710AELP, Omega Optical), and the $[Ca^{2+}]_i$ camera uses a 585 ± 20 nm band pass filter (25 mm round 585AF40, Omega Optical). Both cameras have a lens (25 mm 1 inch format C-mount, Navitar) to which the filters are attached by a custom connector. In this figure, the setup contains two Dalsa cameras for high spatial resolution imaging (DS-12–16K5H, 128 × 128 pixels, typically 487 frames/sec), but with simple changes in the image acquisition control software, either one or both cameras can be replaced with a Redshirt CCD for high temporal resolution (CardioCCD-SMQ, Redshirt Imaging 26 × 26 pixels, 5000 frames/sec). The cameras are supported by a pair of custom mounting plates (12) supported by a tilt and rotation stage (Newport P080N). A 6 mm thick aluminum base plate can accommodate various combinations of lenses and working distances. The entire system is mounted on a 20 cm × 20 cm lab jack that allows the height to be easily adjusted. A custom computer program controls all data acquisition, camera calibration, camera synchronization, laser illumination, and external stimuli.

The diagram of the optical setup configured for concurrent V_m and NADH imaging is displayed in Figure 1B. In this case two light sources, a laser (Verdi, Coherent) and a mercury lamp (Nikon), are utilized. The light from the mercury lamp passes through a 365 ± 5 nm band pass filter (D365/10, Chroma) and is directed to the heart by means of a dichroic mirror (DM1) (400 DCLP, Omega Optical), which transmits the light with a wavelength of >400 nm and reflects the light with a shorter wavelength. The second dichroic mirror (DM2) (495 DCLP, Chroma) deflects the NADH autofluorescence into a 52-mm lens (Fuji) of a Redshirt camera (Camera 1) with an attached 470 ± 20 nm band pass filter (D470/40, Chroma). The fluorescence of the fluorophore is transmitted by DM2 and collected with a 52-mm lens (Fuji) of a Dalsa CCD camera equipped with a 607 nm long pass filter (Red, 607 nm, Tiffen).

Image Registration. For maximum usefulness, the images recorded by the cameras should correlate spatially as well as temporally. The Newport stages allow quick and accurate mechanical alignment. Because the translation stages are expensive, as are the custom machined parts, we developed an alternative to precise mechanical alignment using a numerical algorithm that allows fine image alignment with only very coarse mechanical alignment of the cameras. The breadth of image registration methods is reviewed elsewhere (15); here we address those that have been applied to dual camera cardiac imaging and the simple approach we have adopted.

Direct placement of fiducial reference points on the heart that are visible in both cameras would permit a traditional image registration but interfere with the fluorescence data. Omichi *et al*. (5) reported placing a grid in the field of view to be used for image registration, with a positional accuracy of ± 1 mm. However, in their approach, the two cameras view the heart from different perspectives, which invariably leads to less than ideal image registration.
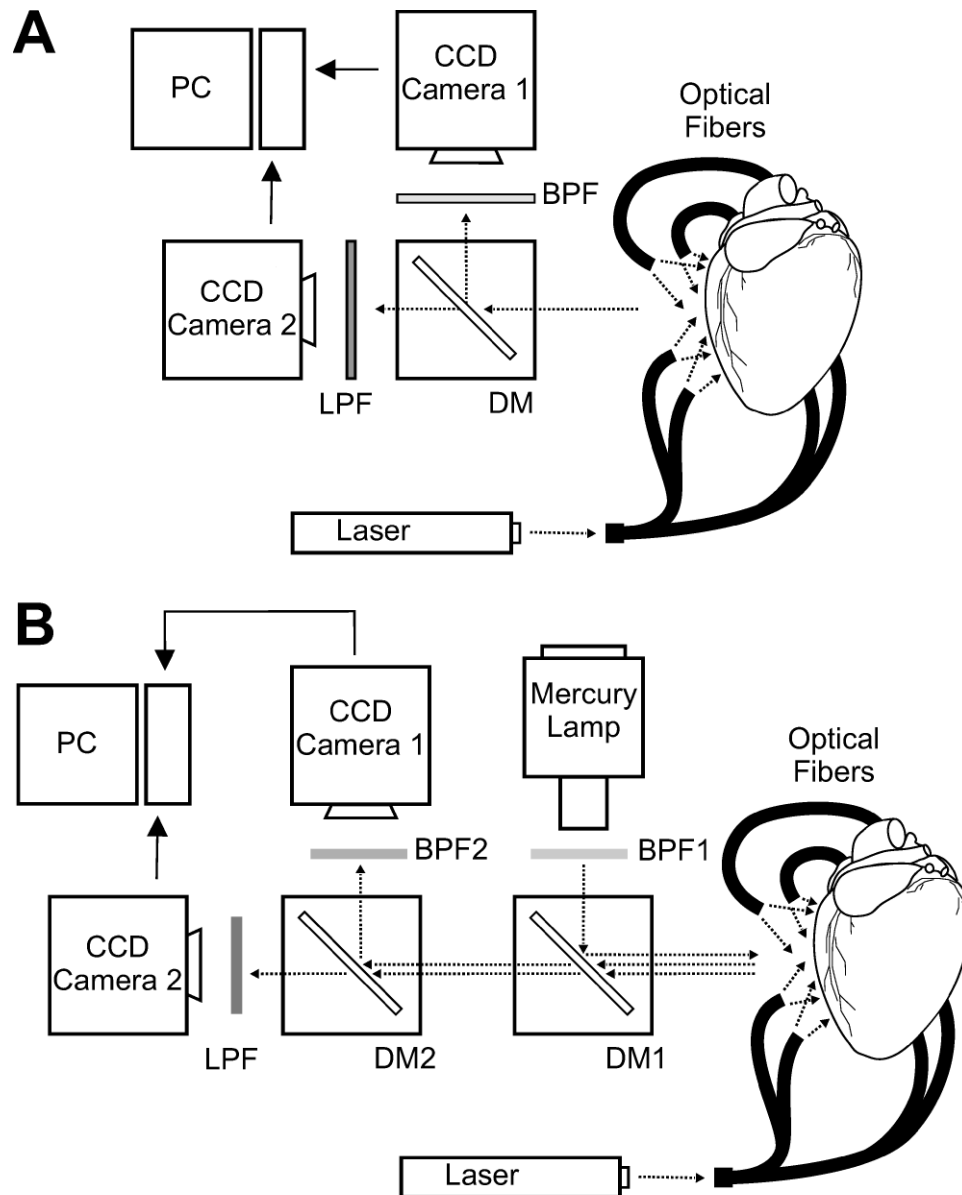
Figure 1. Diagram of our experimental setup configured for simultaneous recording of A: V_m and $[Ca^{2+}]_i$, and B: V_m and NADH. Laser light (532 nm) is delivered to the heart with optical fibers. (A) The dichroic mirror (DM) reflects short-wave (<635 nm) and passes long-wave emitted fluorescence. The band pass (BPF) and long pass (LPF) Omega Optical filters are used to image Ca^{2+} and V_m fluorescence, respectively, with two Dalsa CCD cameras (128 × 128 pixels, 487 frames/sec). (B) Light from the mercury lamp is passed through a band pass filter (BPF1, 365 ± 5 nm) and directed to the heart by means of dichroic mirror 1 (DM1), which reflects light below 400 nm and transmits it above 400 nm (400DCLP, Chroma). The second dichroic mirror (DM2) operates at longer wavelengths to reflect light under 565 nm and transmit above 565 nm (565DCXR, Chroma). The NADH autofluorescence, excited with ultraviolet light from the mercury lamp, passes through DM1 and is reflected by DM2 to CCD camera 1 (Redshirt, 80 × 80 pixels, 1000 frames/sec) equipped with a band pass filter (BPF2, 470 ± 20 nm). The emitted V_m fluorescence passes through the two dichroic mirrors and the long pass filter (LPF, >607 nm) before collection with CCD camera 2 (Dalsa, 128 × 128 pixels, 487 frames/sec). Use of different dyes, illumination, and detection wavelengths would enable imaging of other quantities, such as ROS.

Therefore we chose a camera calibration technique which uses a stand-alone alignment grid of small points, each termed an alignment marker (AM). We used a backlit 35 mm photomask with a rectangular grid of translucent AMs containing 15 AMs in the horizontal direction and 11 AMs in the vertical direction. The size of the grid was matched to the field of view of both cameras for the magnification being used—the grid must be seen entirely and in focus by both cameras. The AMs were circular, with a diameter of approximately 0.15 mm so that the width of each AM will occupy two or three pixels using the 12 mm × 12 mm field of view we used in our experiments. The exact size of the AMs is not critical. A photomask is convenient but not necessary; we have also used a simple grid made on a laser

printer. The exact spacing of the AMs is also not critical since both cameras view the same grid and only their relative positions are used.

Were we to assume that light entering both cameras is paraxial and there is no difference in magnification due to unequal object distances or lenses, we could use a least-squares fit with corresponding alignment points to compute a global offset vector and rotation. We find that the generic method we have developed to correct for local distortions works well without the need for *a priori* assumptions regarding the sources of all distortions in the images. This is particularly important since the source of the largest distortions can change each time the mechanical setup is altered. Our specific camera calibration implementation uses the rubber sheet transformation technique whose salient features are described by Gonzalez *et al.* (16). More sophisticated solutions to the general registration problem have been developed (15), including using radial basis functions (15) or elastic registration (17). The method we have chosen permits correction of distortions and at the same time is computationally simple enough to be applied in real-time. This allows the calibration to be integrated in the acquisition software.

The calibration procedure begins by recording one image with each camera, with the alignment grid in the field of view of both cameras. For each of the two images, we first identify the approximate location of each alignment mark (AM) in an image. To do this automatically we sort all pixels by intensity, while keeping their associated spatial coordinates. The brightest pixel is taken as the approximate location of one of the AMs. All pixels within a distance of five pixels from this pixel are removed from our search for other AMs, as the AM separation is about 10 pixels. With these nearby pixels removed from consideration, the brightest pixel remaining identifies the approximate location of another AM. We repeat this process of selection of the most intense pixel and removal of nearby pixels from the list until the approximate locations of all AMs are found.

Since the AMs are larger than one pixel, we next need to determine accurately the coordinates of the AM geometric centers. Because our AMs are less than two pixels in diameter, we use the 3×3 set of pixels centered around each approximate AM location to determine a center-of-intensity of each AM given by

$$\vec{X} = \frac{\sum_{i=x-1}^{x+1} \sum_{j=y-1}^{y+1} x_{ij}(I_{ij} - B)}{\sum_{i=x-1}^{x+1} \sum_{j=y-1}^{y+1} I_{ij}}, \quad (1)$$

where $\vec{X}$ is the calculated coordinates of the geometric center of the AM, I_{ij} is the intensity of the ij^{th} pixel, and B is the average background intensity of the entire image. In the case where $(I_{ij} - B)$ gives a negative value, it is taken as zero. The approximate center of the AM, (x,y), in the previous step determines the limits of the summations. When the center-of-intensity has been computed for all AMs in both images, the resulting two tables of pairs of floating-point numbers listing the calculated geometric center of all AMs in the alignment grid form the completed correspondence map. We term each entry in a table an alignment point.

Were we to assume that there were no distortions between the two images, we could use a least-squares fit with corresponding alignment points to compute a global offset vector and rotation. However, because of distortions from the lenses and differences in magnification, we find it is better to use the alignment point correspondence map to identify and correct for local distortions. For our experiments, we arbitrarily choose to adjust the V_m image and leave the $[Ca^{2+}]_i$ image unchanged, although it does not matter which image is adjusted. For each of the 16,384 pixels in the V_m image, we locate the closest four V_m alignment points. As illustrated in Figure 2A part 1, we use our knowledge of the grid geometry to locate the corresponding four alignment points in the $[Ca^{2+}]_i$ image, part 2, denoted V_m'. We compute the position of a V_m pixel in relation to the $[Ca^{2+}]_i$ image by calculating the location $\vec{X}'$ in V_m', the processed V_m image, that corresponds to the location (i,j) given by

$$\vec{X}' = \frac{\sum_{k=1}^{4} \vec{r}'_k - (\vec{r}_k - \vec{X}_{ij})}{4}, \quad (2)$$

where $\vec{X}_{ij}$ is the original V_m pixel location, and $\vec{X}'$ is the calculated corresponding point in the V_m' image. $\vec{r}'_k$ and $\vec{r}_k$ are alignment points in the $[Ca^{2+}]_i$ and V_m images, respectively.

Most pixels from the V_m image do not correspond to only one pixel in the V_m' image. Because of distortions, the fractional pixels mapped into a particular pixel in V_m' may not sum to unity. If n pixels from V_m partially map to pixel (i,j) in V_m' with percentages f_n, the intensity of the ij^{th} pixel in V_m' is given by

$$I'_{ij} = \frac{\sum_{k=1}^{n} I_k f_k}{\sum_{k=1}^{n} f_k}. \quad (3)$$

No processing is done on the $[Ca^{2+}]_i$ images other than to eliminate pixels that do not map to V_m'. At the end of this procedure a calibration file is saved that describes how to process the images from both cameras. An interactive program written in C allows the camera calibration to be accomplished very quickly. The same calibration file can be used repeatedly to process movies as long as the cameras are not moved with respect to each other.

To demonstrate our technique, the cameras were
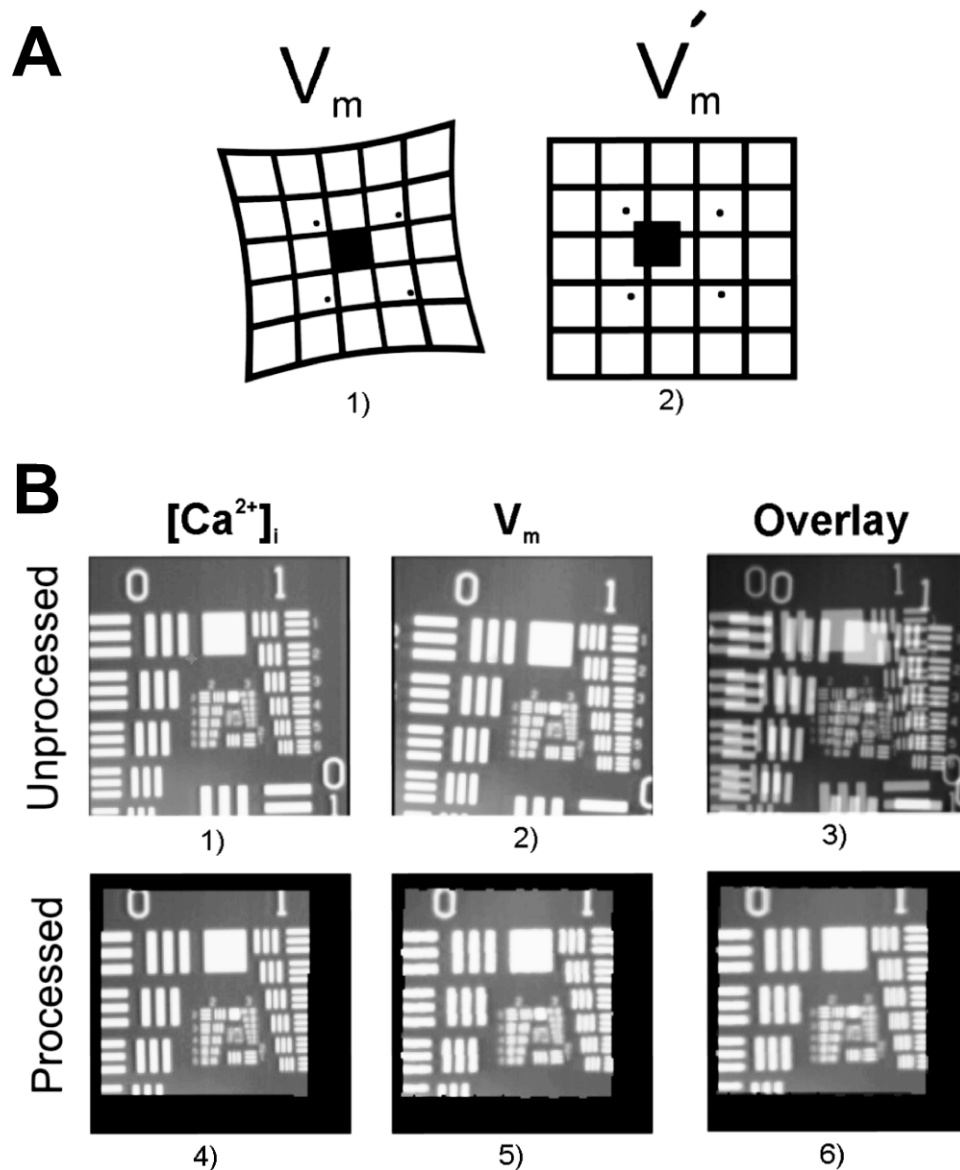
Figure 2. Image registration using the rubber sheet algorithm. (A) Pixel mapping. Left: V_m image; right: V_m' image. A single highlighted pixel in the V_m image with its four closest alignment points (left) is mapped to the image grid V_m' (right) using the corresponding alignment points in the $[Ca^{2+}]_i$ image. (B) Demonstration of numerical alignment of two-camera images. 1) and 2) Unprocessed images from both cameras. 3) Overlay of intentionally misaligned, unprocessed images. 4) and 5) Processed images. 6) Overlay of the processed images. The field of view is approximately 12 mm $\times$ 12 mm.

deliberately misaligned. After completing the calibration procedure just described, we placed a test target in front of the cameras. Images (1) and (2) in Figure 2B are unprocessed and show the test target (USAF 1951 Res Target, Edmund Optics) as seen from both cameras. Image (3) is the combination of the raw images before processing, with one set to 50% transparency. Note that there are significant translational and rotational differences in the two images. Images (4) and (5) were processed using the calibration data. Image (6) shows the combined processed images, with the same one set to 50% transparency; note the significant improvement in this overlay in comparison with the one in (3). In tests in which the cameras were better aligned, the positions of features in the images typically differ by no more than one pixel for the 128×128 pixel image. In the example shown in Figure 2, the processed images differ by as much as two pixels. We believe that the large rotation in this example exposes the weakness of using only linear interpolation, although the results are still quite good.

A disadvantage of the software calibration is that all pixels in the CCD cameras are not utilized since the aligned images can only represent the intersection of what is seen by both cameras. This effect can be seen as the black borders in the processed images (4)–(6) in Figure 2B. A second disadvantage is that the calibration makes no allowance for
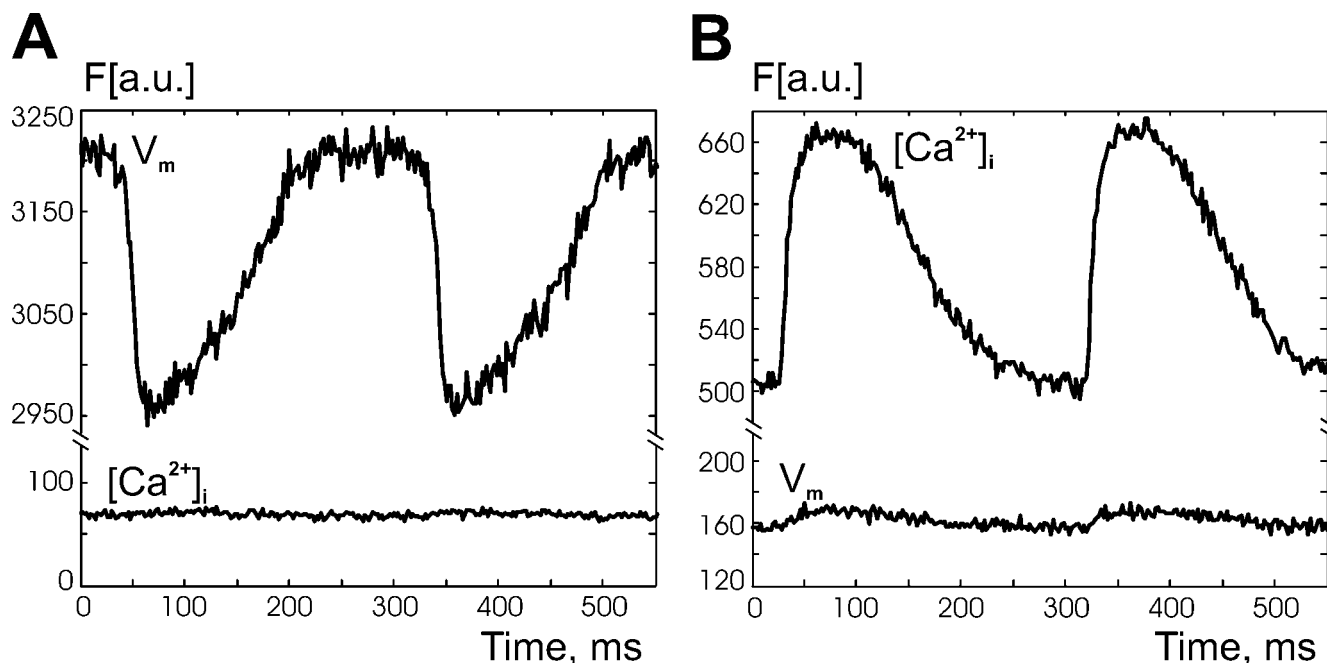
Figure 3. Changes in fluorescence recorded at one pixel when the heart was stained with either RH-237 (A) or Rhod-2 AM (B) alone. (Reprinted from Sidorov *et al.* (18) with kind permission of Springer Science+Business Media.)

surface curvature of the heart, which could affect the mapping of a single point on the heart to the two planar images which were aligned using a planar array of AMs. For the small field of view we typically use, however, this is not a significant problem, but it could be accounted for by using a non-planar alignment grid in the calibration procedure, for example a solid object with AMs (13). The C source code which accomplishes our camera calibration and applies it to images can be found at http://www.vanderbilt.edu/viibre/technologies.htm.

Field Lens for Image Magnification. A field lens arrangement commonly used in these types of imaging studies is easily configured by attaching a positive achromatic lens (15 mm, Omega Optical) to the cubical mirror housing (NT56–265, Edmund, not shown in Fig. 1), such that the lens is now the first element in the dual camera system. We can magnify and narrow the field of view to be as small as 2 mm $\times$ 2 mm, which would be required to image, for example, a mouse heart. In adjusting the various parameters, we found that focusing the 25 mm lenses to infinity and adjusting the camera distance from the mirror-lens combination works best for controlling the field of view. Varying the distance between the entire system and the heart works best for adjusting focus. This configuration achieves a small field of view without losing a significant amount of light and preserves the shallow depth of field that is important in this type of imaging.

Spectral Overlap Estimation of RH-237 and Rhod-2 AM. To estimate the spectral overlap between RH-237 and Rhod-2 AM fluorescence, we followed two separate experimental protocols that we have published

previously (18). In the first protocol at the beginning of the experiment the heart was stained only with the V_m-sensitive dye RH-237 and both voltage and "calcium" images were recorded using the respective filters. The data acquired through the calcium filter represented the bleed-through of the voltage signal, which we termed the calcium error (error $[Ca^{2+}]_i$). Thereafter the Ca^{2+}-sensitive dye Rhod-2 AM was administered, and data were acquired while the heart was continuously stimulated at a pacing rate of 300 ms. In the second experimental protocol only Rhod-2 AM was used at first. In this situation, the "voltage" images represented the voltage error (error V_m). After collecting data, the heart was then stained with RH-237, the pacing protocol was repeated, and voltage and calcium fluorescence were recorded again. To calculate the error due to overlap of the voltage and calcium spectra, the amplitude of the calcium transient error was normalized to the amplitude of $[Ca^{2+}]_i$:

$$\% error[Ca^{2+}]_i = \frac{error[Ca^{2+}]_i}{[Ca^{2+}]_i} \times 100\%.$$

The error for voltage measurements was calculated as the amplitude of the voltage error normalized to the amplitude of the V_m signal:

$$\% error V_m = \frac{error V_m}{V_m} \times 100\%.$$

Experimental Preparation. All experiments were conducted in accordance with the National Institutes of Health regulations for the ethical use of animals in research and were approved in advance by the Vanderbilt Institutional Animal Care and Use Committee. New Zealand white
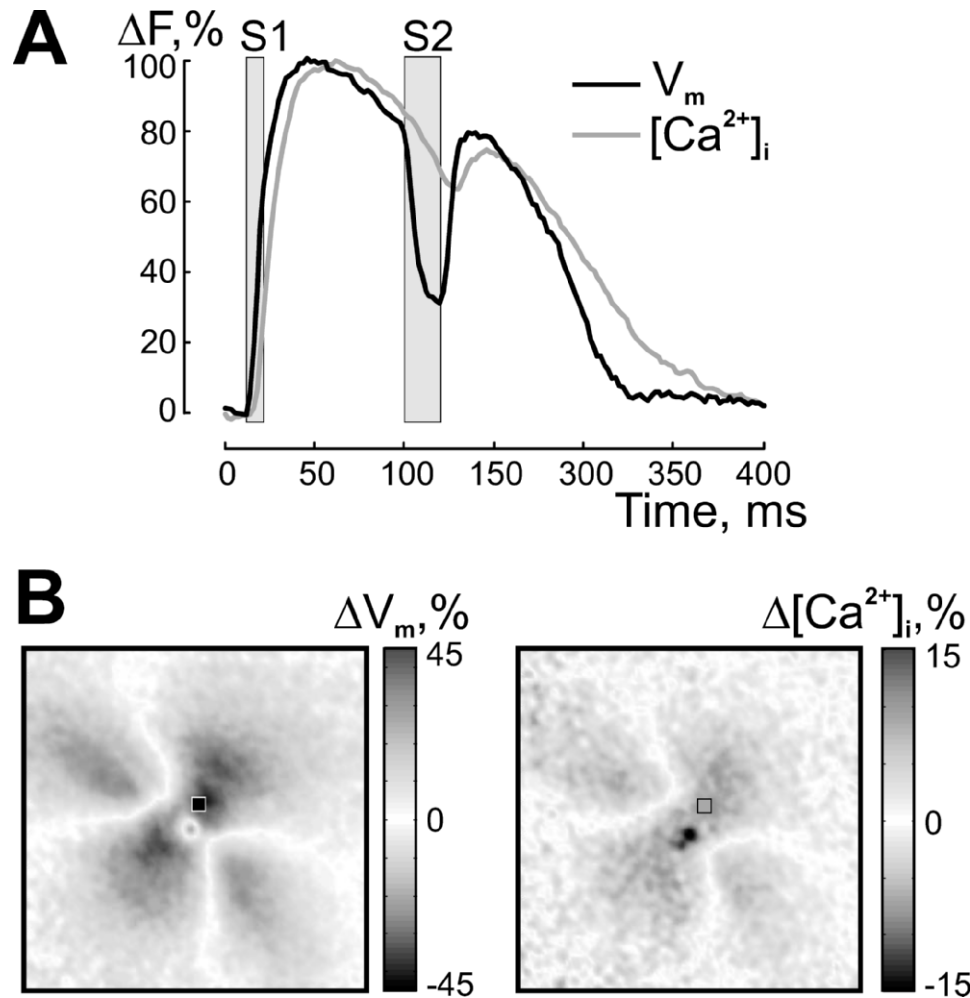
Figure 4. The voltage and calcium responses to anodal stimulation for a 12 mm × 12 mm field of view of the epicardium of an isolated rabbit heart. The S2 stimulus was 20 ms in duration and 20 mA in amplitude and was delivered at an S1–S2 interval of 90 ms. The optical data were first preprocessed by applying a spatial 8 × 8 Gaussian filter and a 3-point mean temporal filter, then normalized on a pixel-by-pixel basis, and are presented as the percentage of highest change in fluorescence. (A) Action potential (black trace) and calcium transient (gray trace) extracted from the same pixel (black and gray squares in (B)) at the central hyperpolarized area. (B) Voltage and calcium distributions at the end of S2. To display net voltage (ΔV_m) and calcium $\Delta[Ca^{2+}]_i$ displacements due to S2, the previous response was subtracted from the S2 response.

rabbits of either sex weighing 2.7 to 3.1 kg were used in the experiments. The detailed description of the heart preparation has been published previously (19). The animals were preanesthetized with ketamine (50 mg/kg), heparinized (1,000 units), and anesthetized with sodium pentobarbital (60 mg/kg). The heart was quickly removed from the chest and mounted on a Langendorff apparatus for retrograde perfusion with oxygenated Tyrode's solution of the following composition (mM): 133 NaCl, 4 KCl, 2 CaCl$_2$, 1 MgCl$_2$, 1.5 NaH$_2$PO$_4$, 20 NaHCO$_3$, and 10 glucose. For experimental protocols where endocardial imaging was required, the right ventricle was isolated from the rest of the rabbit heart, stretched across a Plexiglas frame, and cannulated via the right coronary artery (20). All experiments utilized either a commercial current source (Bloom), custom USB-powered and -controlled stimulators (21), or a custom high-voltage stimulator (22).

Fluorescent Dye Staining. We have used our dual camera system in a variety of experimental protocols that demonstrate the capabilities of the approach. Unless otherwise noted, the excitation-contraction uncoupler 2,3-butanedione monoxime (BDM, Sigma-Aldrich, St. Louis, MO) was added to the perfusate (15 mM) to eliminate contractile optical artifacts. For field-shock, trabecula experiments, and simultaneous V$_m$ and NADH measurements, the heart or right ventricle preparation was placed in a bath; otherwise the heart was in air. The first experiments using this system were studies of simultaneous V$_m$ and [Ca^{2+}]$_i$ on the anterior left ventricle of a Langendorff-perfused rabbit heart in response to unipolar cathodal and anodal stimulations (18). In these experiments, the heart was first stained with the calcium-sensitive dye Rhod-2 AM by delivering slowly 1 ml of the dye stock solution (0.5 mg/ml DMSO) via an injection port above the aorta. Thereafter, 10
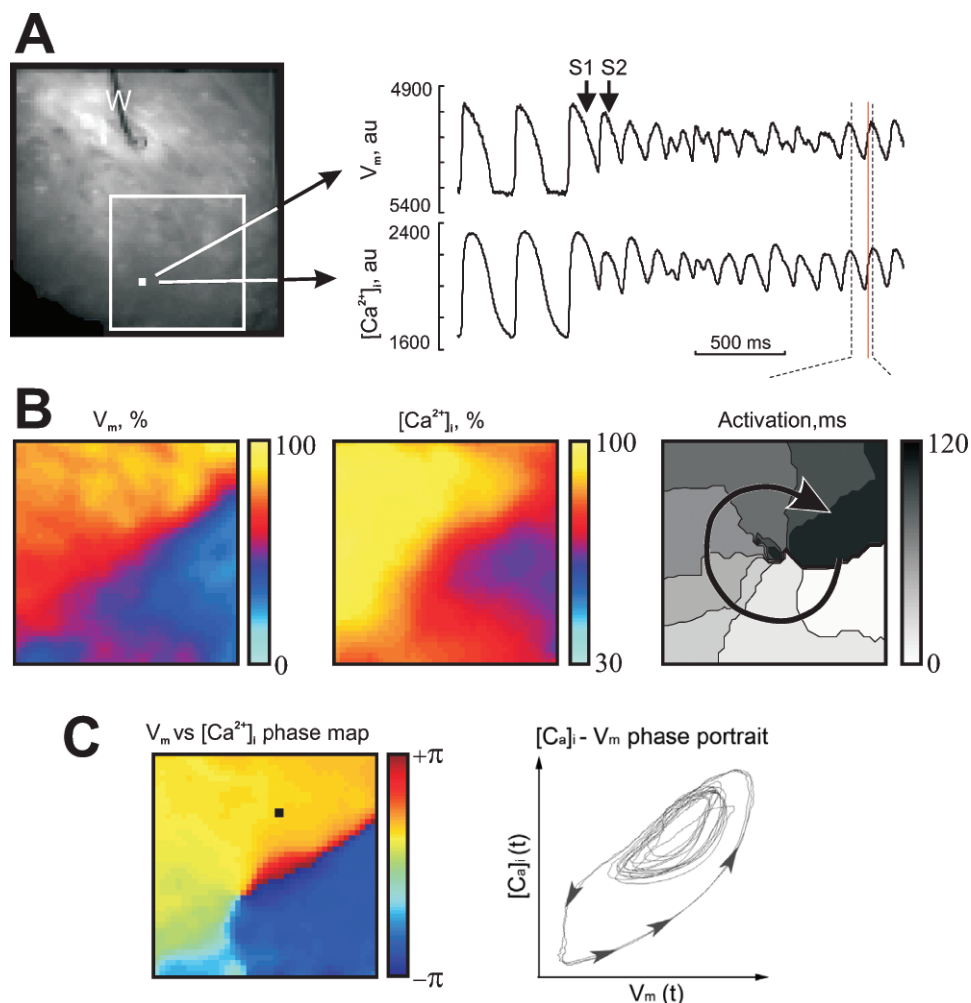
Figure 5. The voltage and calcium dynamics in the isolated right ventricle preparation. (A) The arrhythmia was initiated by two premature stimuli (S1, S2) delivered via a wire electrode (W). The image size is 22×22 mm^2. During the last 400 ms the stationary rotor with its center located inside the white square drives the arrhythmia. Two traces represent RH 237 and Rhod-2 AM fluorescence. (B) and (C) demonstrate data analyses from the open white square in (A). The left and middle panels of (B) show the spatial distributions of V_m and $[Ca^{2+}]_i$ for the 2314 ms time point, indicated by the red line in the temporal traces in (A). The activation map on the right shows one complete rotation with time resolution of 15 ms. The left panel of (C) shows the V_m versus $[Ca^{2+}]_i$ phase map at 2314 ms, while the right panel of (C) is the phase-space trajectory over time for the black pixel in the phase map for the entire duration of recording, 2468 ms (at 1000 frames/sec).

μl of the voltage-sensitive dye RH-237 (1 mg/ml DMSO) was gradually administered through the same injection port. In other experiments in which V_m alone was imaged, the heart was either stained with RH-237 as described above or with another voltage-sensitive dye, di-4-ANEPPS (200 μl of stock solution with concentration of 0.5 mg/ml DMSO). In concurrent V_m and NADH recordings, di-4-ANEPPS was used. Ratiometry experiments utilized RH-237. Both anoxia and ratiometry experiments were conducted without an excitation-contraction uncoupler. Hearts were loaded with dihydroethidium (DHE), an indicator of reactive oxygen species (ROS), by recirculating Tyrode's solution containing 6.34 μM DHE in the perfusion system for 20 minutes, followed by a washout period of 25 minutes with standard Tyrode's solution. In all experiments the fluorescent dyes were excited by 532 nm laser light (Verdi, Coherent, Santa

Clara, CA), although it is also possible to use other light sources, including light emitting diodes (12, 23, 24).

Fluorophore Emission Spectra. To compare the emission spectra of DHE as a reporter of ROS, Rhod-2 AM as an indicator of $[Ca^{2+}]_i$, and di-4-ANEPPS and RH-237 as indicators of V_m, we used 532 nm laser light for excitation. A USB2000 miniature fiber optic spectrometer (Ocean Optics, FL, USA) was used to record the fluorescence spectra of the different probes. The spectrometer comprises optical elements coupled with a 2048-element linear silicon CCD array detector which is responsive from 200 to 1100 nm.

NADH Imaging. As an important part of our multi-modal cardiac imaging (MCI), we also demonstrate the feasibility of NADH imaging in both single and dual camera configurations. In particular, these cameras can be utilized to image ischemia-related changes in the concentration of reduced nicotinamide adenine dinucleotide (NADH), which
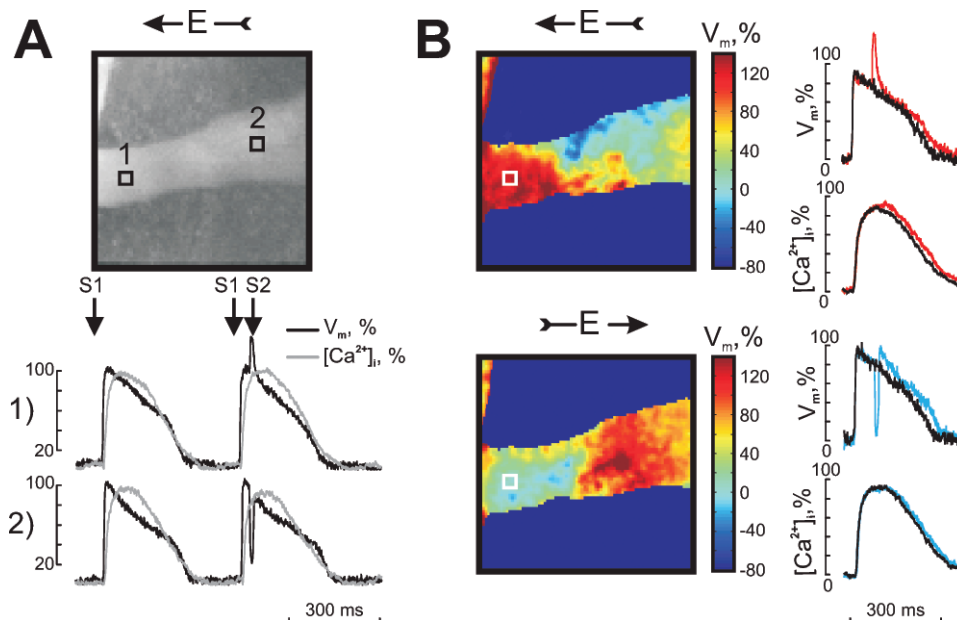
Figure 6. The response of a right ventricular trabecula to field stimulation. Two high-speed Redshirt CCD cameras were used to acquire the data. An achromatic lens was added to the dual camera system to obtain the small 5×5 mm^2 field of view shown in the top image of panel A. The preparation was stained with RH 237 and Rhod-2 AM to image V_m and $[Ca^{2+}]_i$, respectively, using filters as described in the text. (A) The trabecula response to field shock of 10 ms duration and 20 V/cm strength at an S1–S2 interval of 70 ms. The time traces 1) and 2) show the averaged responses from the areas depicted by the "1" and "2" squares in the image. (B) The V_m distribution during negative and positive field stimulation of 30 V/cm at a coupling interval of 100 ms. The averaged traces from one square (white) illustrate the tissue responses as a function of shock polarity. The traces from the virtual cathode (red) and virtual anode (blue) are superimposed on the optical signals recorded when only the S1 field shock was applied. The optical data were preprocessed with a spatial 5×5 Gaussian filter and normalized. The arrow above the image indicates electric field direction. The spatial and temporal resolutions are 80×80 pixels and 1000 frames/sec, respectively.

plays a critical role in the mitochondrial generation of ATP. NADH is autofluorescent—it absorbs light in the ultraviolet range of 320–380 nm and emits fluorescence between 420–480 nm. The oxidized form (NAD$^+$), however, does not absorb light in the 320–380 nm range. Thus imaging NADH gives a measure of the redox state of the mitochondria (25). To spatiotemporally measure NADH, light from a mercury lamp (Nikon) was passed through a 365 ± 5 nm band pass filter and directed onto the surface of the isolated heart via a dichroic mirror. The emitted light was band pass filtered at 470 ± 20 nm before being collected by a CCD camera.

Results

Estimation of Spectral Overlap of RH-237 and Rhod-2 AM. Figures 3A and 3B demonstrate the fluorescence recordings when hearts were stained with either RH-237 or Rhod-2 AM, respectively (18). No prominent RH-237 fluorescence bleeding through the band pass filter is observed in Figure 3A (lower trace). The mean % error of $[Ca^{2+}]_i$ was 3.97 ± 1.66 (3 hearts). If the heart was stained only with Rhod-2 AM (Fig. 3B), slight leakage of $[Ca^{2+}]_i$ fluorescence through the long pass filter is observed (lower trace). The mean % error of V_m was 4.45 ± 1.94 (3 hearts).

Dual V_m and $[Ca^{2+}]_i$ Imaging. Figure 4 shows the V_m and $[Ca^{2+}]_i$ responses to a strong systolic stimulus (S2) applied to an isolated rabbit heart. A detailed discussion of these data is beyond the scope of this paper and is presented

elsewhere (18), but the figure does show the ability to distinguish the detailed spatiotemporal relationship of the two signals. Briefly, it is well established that V_m leads $[Ca^{2+}]_i$ during normal pacing (S1 stimulation), as shown in Figure 4A. Figure 4B clearly demonstrates the interesting feature that upon termination of the S2 stimulus, the $[Ca^{2+}]_i$ distribution correlates spatially with the virtual-electrode V_m polarization pattern for an S1–S2 coupling interval of 90 ms, although as shown by the scale bars, the magnitude of the peak-to-peak excursion in the $[Ca^{2+}]_i$ signal is smaller than the peak-to-peak difference observed in V_m (also evident for the single pixel time traces shown in Fig. 4A).

One of the important applications of the dual camera system is the study of the V_m and $[Ca^{2+}]_i$ relationship during an arrhythmia. Figure 5 displays an example of the spatiotemporal dynamics of V_m and $[Ca^{2+}]_i$ during reentry initiated in the isolated right ventricle of a rabbit heart. The analyzed interval corresponds to the time segment when the stationary rotor located inside the white square of the image in Figure 5A drives the arrhythmia. The snapshots of V_m and $[Ca^{2+}]_i$ distributions and an activation map of one complete rotation are shown in Figure 5B. Figure 5C demonstrates the ability of dual camera imaging of V_m and $[Ca^{2+}]_i$ to quantify the instantaneous phase of the heart, without having to rely on time-delay embedding (1, 2). To create the V_m versus $[Ca^{2+}]_i$ phase map in the left panel of Figure 5C, we calculated the phase angle as arctan ($[Ca^{2+}]_i$/

A
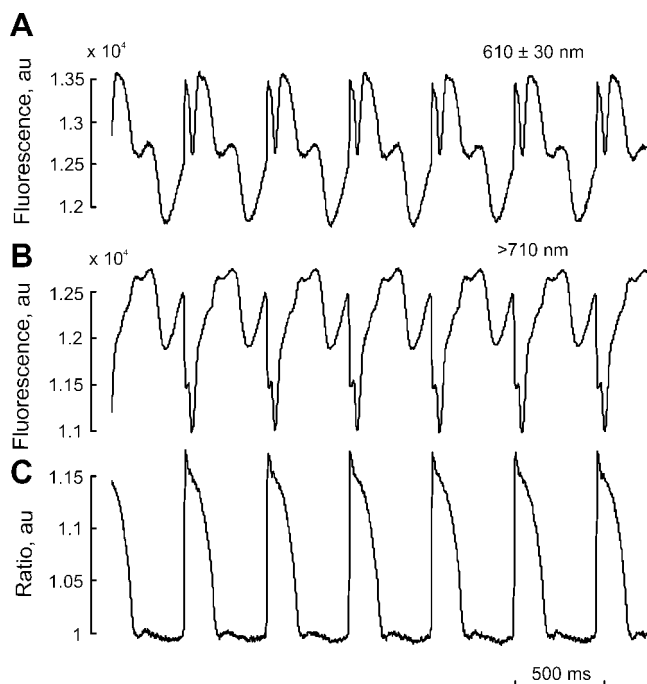
Figure 7. Ratiometric measurement of optical action potential. The heart was stained with RH-237 and illuminated with laser light (532 nm). To split the emission light, we utilized a beam splitter with 70% reflectance and 30% transmission. Two high-speed Redshirt CCD cameras were used to image: (A) short- (610 ± 30 nm) and (B) long-wave (>710 nm) fluorescence. (C) The ratio of short- (A) to long-wave (B) fluorescence. The data were filtered with a spatial 5×5 Gaussian filter and a 5-point mean temporal filter. The spatial and temporal resolutions were 80×80 pixels and 1000 frames/sec, respectively. The gain for the camera recording short-wave fluorescence was 10 dB, and for the camera recording the long-wave signal the gain was 3 dB.

V_m). On the right of panel C, the phase-space trajectory (1, 26) is shown for the black pixel in the phase map. The change in the shape, size, and center of the trajectories reflects the onset of the higher-frequency reentrant arrhythmia following S2.

Field Lens Magnification of Trabecula. As a demonstration of the ability of the system to capture high-resolution dual images using the field lens arrangement, Figure 6 shows a 5×5 mm^2 image of a trabecula from an isolated right ventricle of a rabbit heart. The V_m and $[Ca^{2+}]_i$ traces in panel A illustrate the tissue response during continuous pacing (S1) and uniform field shock (S2, 20 V/cm, S1–S2 interval of 70 ms) at opposite ends of the trabecula. Figure 6B illustrates the effect of field polarity (-30 V/cm and $+30$ V/cm, S1–S2 interval of 100 ms) on tissue response at one location. By using an opaque piece of black paper to shield the trabecula from the underlying tissue (27), we avoided contamination of the images by the fluorescence of the underlying tissue. The field-induced polarization is clearly seen in optical traces from opposite ends of the trabecula, showing opposite polarities of shock-induced changes in V_m.

Ratiometry. The motion artifact occurs by means of several mechanisms. Among the most important are the movement of the cardiac tissue from the registration field of one detector element into the field of view of the neighboring element, and the change in wavelength-dependent light scattering and transmission due to tissue contraction (28). Ratiometry using reflected excitation light or fluorescence as a reference can be very valuable in suppressing the motion artifact (28–31). Our system is an ideal setup for ratiometric imaging of V_m, in which only the filters need to be changed. Figure 7 demonstrates optical signals acquired with a 610 ± 30 nm band pass filter (Fig. 7A) and 710 nm long pass filter (Fig. 7B). The short/long wave fluorescence ratio significantly reduces the motion artifact (Fig. 7C).

Because the cardiac tissue moves with regard to exciting and detection optics, the time-space analysis is an advantageous approach for motion quantification. Figure 8 illustrates such a technique for estimation of the motion dimensions along the two space axes that intersect at a chosen pixel, whose optical traces were presented in Figure 7. We show a heart image in Figure 8A and time-space plots in Figures 8B and 8D. The motion waves are evident in the space derivative maps (panels C and E). The crest positions of the motion waves marked with white curved lines show motion deflections occurring at the spatial scale of less than 2 mm. Figure 8F also displays short-wave (upper dashed trace) and long-wave fluorescent recordings (lower dashed trace) bearing both V_m signal and motion artifact and superimposed short/long ratiometric signals (black traces). The subtraction of the short-wave and black traces and the long-wave and black traces demonstrates almost identical motion artifacts (upper and lower gray traces).

We anticipate the ease of acquiring ratiometric measurements with this system will be particularly important in metabolic imaging experiments since the use of contraction blockers can result in a large reduction of cardiac metabolic demand, and, hence, it is important to develop practical techniques to reduce motion artifact.

Dual-Rate Imaging. We have also used this system with one low-resolution, high-speed camera running at 5000 frames/sec (26×26 pixels, CardioCCD-SMQ, Redshirt Imaging) and one high spatial resolution camera (DS-12–16K5H, 128×128 pixels, 487 frames/sec, Dalsa) in a field shock study. In this case the heart was stained with only a voltage dye (di-4-ANEPPS), and both cameras used the same long pass filters (>607 nm). The dichroic mirror was replaced with a 70% transmission/30% reflection beam splitter which allowed both cameras to view the same activity. Figures 9A and B show the whole heart as acquired with the Redshirt and Dalsa CCDs, respectively. Comparing the high temporal resolution Redshirt fluorescence data in Figure 9C with the high spatial resolution Dalsa data in Figure 9D reveals how much activation information is lost in the Dalsa data. Prominent positive polarization of the right ventricle and negative polarization of the left ventricle
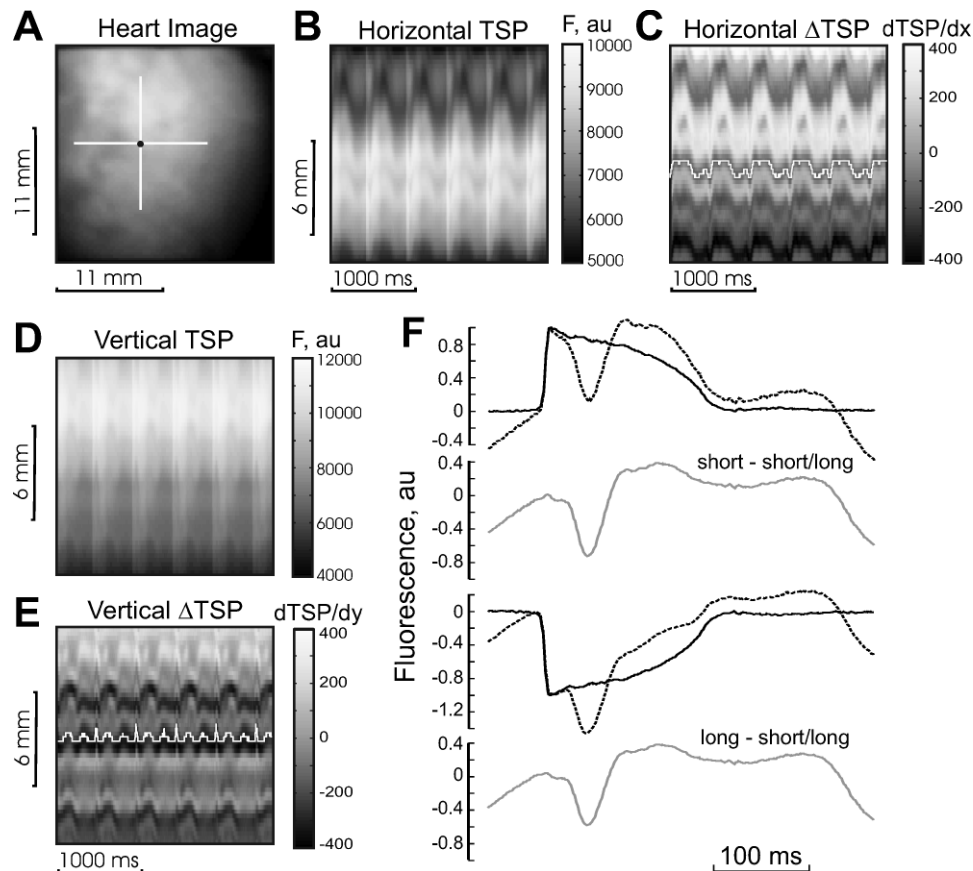
Figure 8. Motion amplitude quantification in the ratiometric determination of V_m. (A) Heart image. (B) and (D) Time-space plots were created along horizontal and vertical white lines centered at the pixel of interest (black dot). (C) and (E) To estimate the extent of motion deflections, the time-space plots were differentiated along the space axis. The white curved lines in the horizontal and vertical differentiated time-space plots represent crest positions of motion waves in the vicinity of the black pixel. (F) The time (dashed) traces are a 400-ms long interval of the recordings from Figure 7 showing short- (Fig. 7A) and long-wave fluorescence (Fig. 7B) with superimposed short/long ratiometric (black) signals (Fig. 7C). The upper and lower gray traces are results of subtractions of the short-wave dashed and superimposed black signals and of the long-wave dashed and black traces, respectively, and, hence, depict traces that reflect the motion without the V_m signal.

are apparent in panel C, whereas in panel D this left/right disparity is reduced to a single frame. Simultaneous acquisition with a Dalsa and a Redshirt CCD is a powerful combination that allows analyses of both high spatial and high temporal information of the same imaging parameter.

Dual V_m and NADH Imaging. Before assembling the dual V_m and NADH imaging system, we conducted several experiments using a single Redshirt camera to validate the feasibility of NADH imaging. Figure 10 provides a demonstration of the type of results that can be obtained with CCD imaging of NADH changes with ischemia and reperfusion. After 30 minutes of global anoxia, the autofluorescence is markedly brighter, indicating an increase in NADH. After reperfusion with oxygenated perfusate, NADH autofluorescence quickly decreases. These results correlate well with previous investigations (25, 32). Because the autofluorescent spectra of NADH do not overlap with the spectra of many of the other optical probes, it is possible to image NADH and $[Ca^{2+}]_i$ (33) and NADH and V_m (34) in the same heart.

Figure 11 portrays an example of data obtained in the dual camera setup (Fig. 1B). The V_m and NADH were imaged by Dalsa and Redshirt cameras, respectively. The optical traces from V_m and NADH data sets extracted from the same location (small black square in panel A) are displayed in Figure 11B. The NADH baseline changes dramatically between the control and anoxia recordings, whereas the individual normalized V_m traces display the significant changes in the shape of action potentials. This reflects the slower mitochondrial dynamics as compared to V_m dynamics of sarcolemma. As shown by the data presented in Figure 10, anoxia induced a substantial increase in NADH autofluorescence (Fig. 11D and 11E). The activation pattern during sinus rhythm illustrated in Figure 11C becomes fragmented and activation delays after 12 minutes of anoxia.

We note that Mayevsky and Rogatsky (25) review the difficulties encountered with NADH imaging in blood-perfused hearts because the absorption/emission spectra of hemoglobin overlap those of NADH. Our ability to image multiple metabolic variables will allow us to assess the
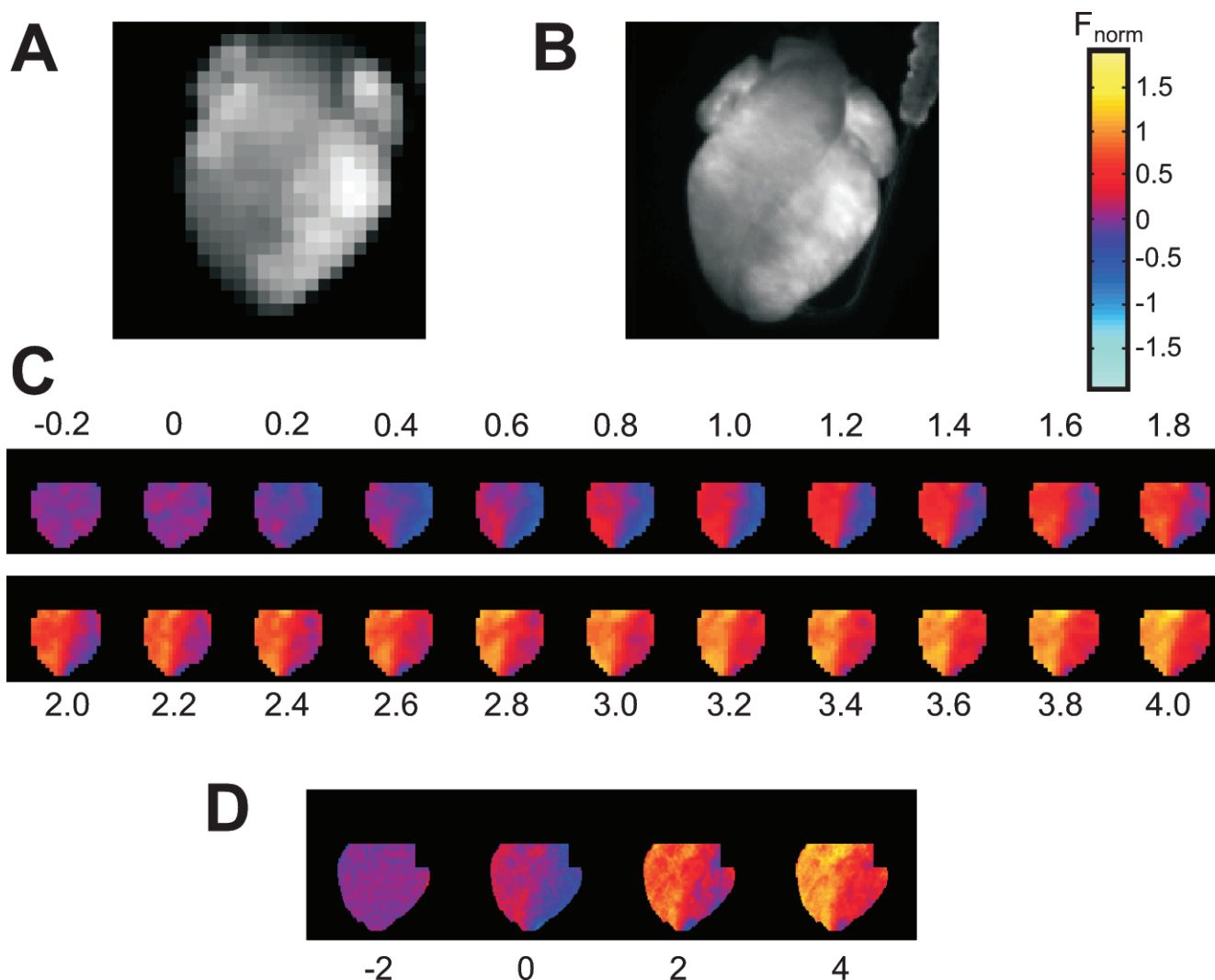
Figure 9. Whole heart field stimulation data acquired simultaneously with high temporal and high spatial resolutions using the dual camera system. The heart was stained with di-4-ANEPPS to image V_m. Raw images of the whole heart were acquired with (A) Redshirt CCD (26×26 pixels, 5000 frames/sec) and with (B) Dalsa CCD (128×128 pixels, 487 frames/sec). In both (A) and (B) the scale is approximately 50×50 mm^2. The insulated bipolar electrode used to pace the heart near the apex can be seen in the right of (B). False color fluorescence (C) Redshirt and (D) Dalsa data reveal the spatiotemporal response of the heart to diastolic field stimulation of 50 V/cm strength and 8 ms duration. The numbers above or below each frame represent the time in [ms] since the field shock onset. The fluorescence data were normalized (F_{norm}) according to the paced beat preceding the field shock. Pixels corresponding to atrial tissue were digitally removed from the images in (C) and (D).

magnitude of the metabolic compromises of non-blood perfusion.

Other Fluorescent Parameters. This dual camera setup can additionally be used for imaging of $[K^+]_e$ (Guy Salama, Personal Communication), NADH (25, 35), and ROS (36, 37) by changing only the optical filters and possibly the excitation source from those used for V_m and $[Ca^{2+}]_i$. Dihydroethidium (DHE) is a membrane-permeable dye that is oxidized preferentially by O^{2-} to form ethidium when inside the cells, which then stains the cell nuclei, emitting a red fluorescence that reports the ROS concentration. Given that spectra of fluorescent dyes are reported commercially for various solvents, Figure 12 allows comparison of the emission spectra of DHE, Rhod-2 AM,

di-4-ANEPPS, and RH-237 as measured in an isolated rabbit heart. With our two-camera system, we can readily image two quantities simultaneously, consistent with the various excitation/emission wavelengths presented in Table 1.

Discussion

Research in cardiac electrophysiology (CEP) tends to focus at two divergent spatial scales—that of the ion channel and the whole heart. Patch-clamp studies of the molecular cardiology of voltage-gated ion channels have the goal of identifying targets for antiarrhythmic drugs and enabling and motivating the development of numerical models of the cardiac action potential in the whole heart.
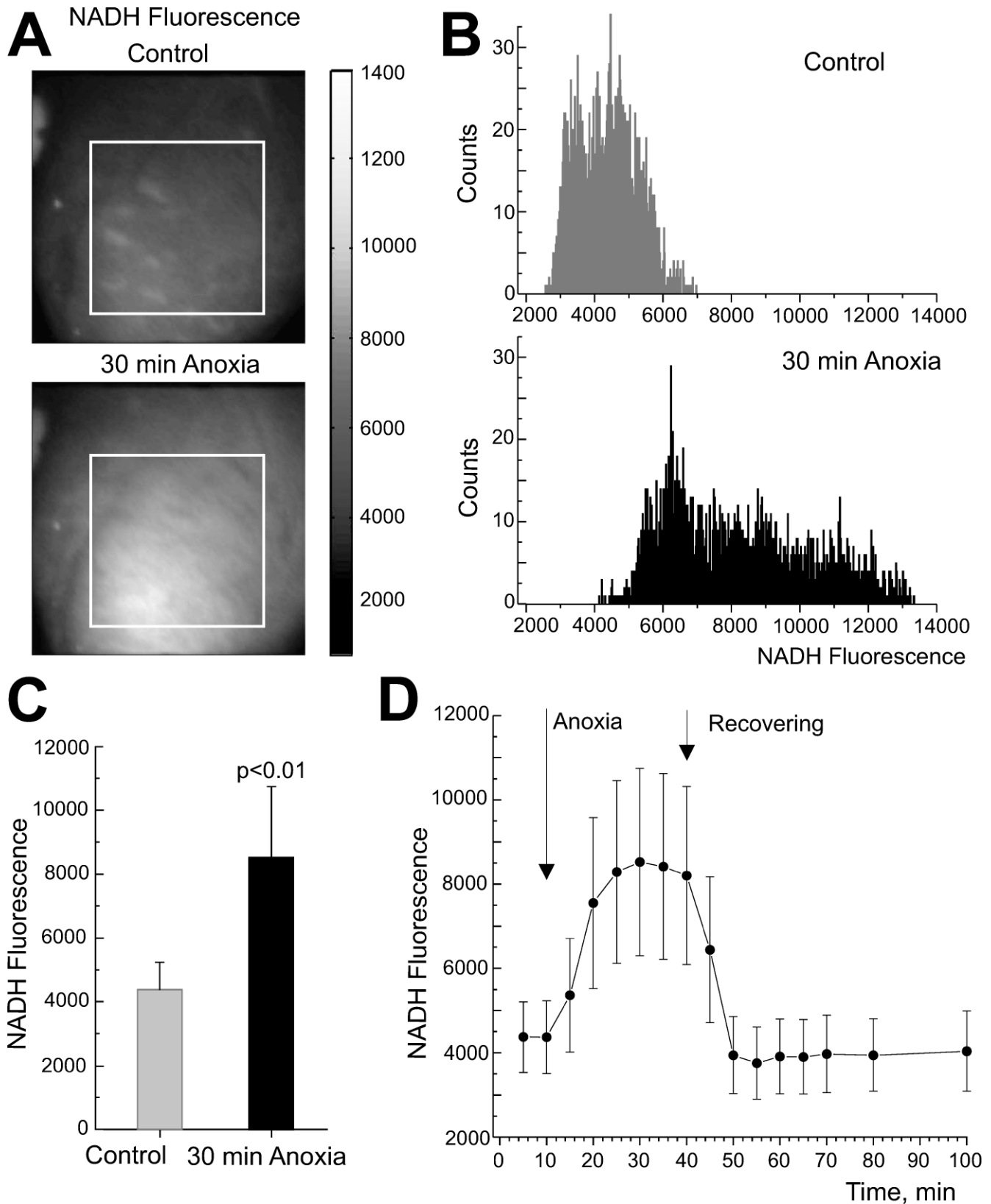
Figure 10. NADH autofluorescence in a Langendorff-perfused rabbit heart under normal conditions (95% O_2 and 5% CO_2) (control) and after 30 minutes of global anoxia (95% N_2, 5% CO_2). (A) Images of the 22×22 mm^2 (80×80 pixels) field of view. (B) Pixel intensity histogram. (C) Histogram integrals demonstrating a statistically significant increase in NADH during anoxia. (D) NADH autofluorescence over the course of the experiment, including control, 30 minutes of global anoxia, and reperfusion.
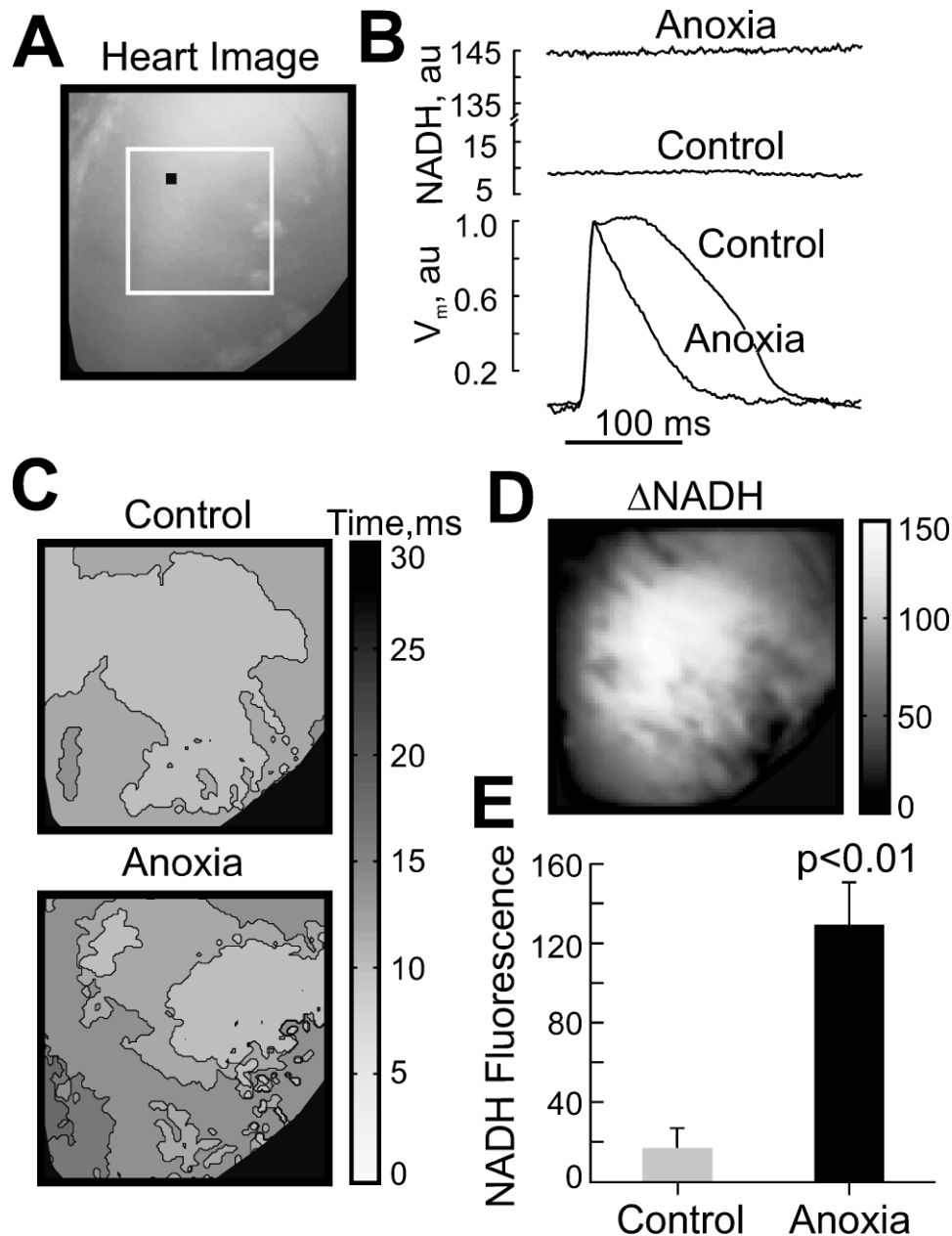
Figure 11. The simultaneous V_m and NADH recording during control (95% O_2 and 5% CO_2) and anoxia (95% N_2, 5% CO_2). (A) Heart image without filtering. (B) V_m and NADH optical traces in control and after 12 minutes of anoxia extracted from the black pixel in panel A. Note the shift in NADH autofluorescence from 9 counts for control to 134 counts for anoxia. (C) V_m activation maps. (D) NADH difference image. (E) NADH autofluorescence integrated over the white square in panel A during control and after 12 minutes of anoxia.

Studies of the whole heart, most recently using fluorescent imaging of the transmembrane potential and intracellular calcium, are directed towards validation of these models, identification of the macroscopic mechanisms of cardiac reentry and fibrillation, and the response of the heart to pacing and defibrillation shocks. Despite these efforts, reentrant cardiac arrhythmias, sudden cardiac death (SCD), and congestive heart failure remain difficult to treat (38–40). The efficacy of many antiarrhythmic drugs has been questioned, in part because of patient-specific pharmacogenetics (41–46). Hence, the prophylactic treatment of choice

for SCD remains the implantable cardioverter/defibrillator (ICD). While the ICD has reduced mortality or morbidity in selected populations (47–52), its prophylactic application in a variety of cardiac disorders has yet to be demonstrated. The challenge in developing new treatments for cardiac disease is to understand the spatiotemporal complexity of ischemic heart disease and heart failure, which can best be addressed with new multimodal measurements and integrated mathematical models. One might ask whether optical measurements of voltage or calcium alone are sufficient for this task. Obviously, the ability of two-camera systems, such
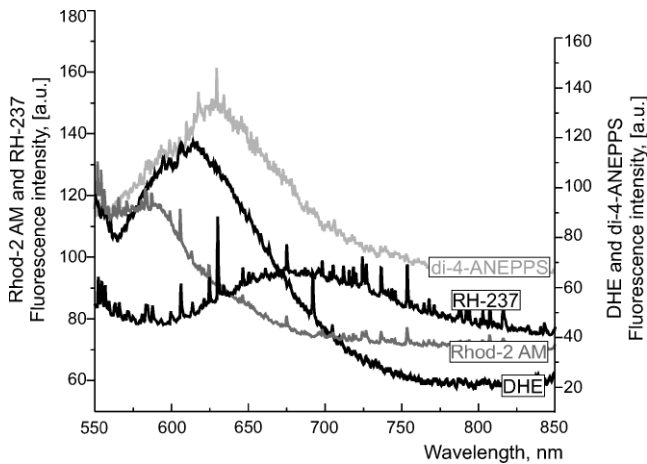
Figure 12. A comparison of the emission spectra measured from a rabbit heart for DHE as a reporter of ROS, Rhod-2 AM as an indicator of $[Ca^{2+}]_i$, and di-4-ANEPPS and RH-237 as indicators of V_m.

as the one we report, to record both variables simultaneously is a step forward.

Looking beyond voltage and calcium, the larger issue is the extent to which other signals are relevant. It is becoming increasingly appreciated that metabolic factors play a role in SCD through their tight interrelationship with CEP (46, 53), and that identification of these factors will strengthen our mechanistic understanding of rate-dependent cardiac re-modeling, heart failure, and fatal arrhythmias, as well as lead to new therapies (54). However, few scientists working on the measurement and modeling of whole-heart CEP have

the tools needed to correlate recordings of spatiotemporal patterns of cardiac activity with measures of metabolism that may affect, or even define, arrhythmogenic substrates.

There is extensive literature on the metabolism of the entire heart and individual cardiomyocytes; there is also a recent growing interest in the quantitative relationships between cardiac metabolism and the ischemic action potential. Recent studies have shown that the ROS associated with ischemia also produce lipid peroxidation products that have a direct effect on ion channel conductances, thereby producing a previously unrecognized coupling between CEP and metabolism (55, 56). What is missing is the ability to correlate spatial patterns of metabolism with those of electrical activity associated with spatial heterogeneities (*e.g.,* regional ischemia), and potentially fatal arrhythmias—an ability that would enable the testing of hypotheses regarding metabolic interventions to reduce the risk of fatal arrhythmias. Hence there is a need to implement technological innovations that will allow the integration of state-of-the-art electrophysiological imaging of the isolated rabbit heart with optical imaging of the metabolism associated with both regional ischemia and tachycardia, *i.e.,* to create correlative MCI.

The challenges of the optical approaches to MCI are related to overlap of the emission spectra of the various dyes and tissue autofluorescence, as illustrated in Figure 13. There are several possible ways that these might be addressed, ranging from development of new dyes (57–59), careful selection of narrow-band excitation and filters,

Table 1. Excitation and Emission Parameters for Correlative Multimodal Cardiac Imaging

| Optical probe	Measured parameter	Excitation maximum (nm)	Recommended excitation (nm)	Emission maximum (nm)	Recommended emission collection (nm)	References
Dihydroethidium (DHE) (oxidized to ethidium)	ROS (O_2^-)	518	532	605	>607 605 ± 25	Invitrogen Invitrogen
Rhod-2 AM	$[Ca^{2+}]_i$	550	532	571	585 ± 20	Invitrogen
Di-4-ANEPPS	V_m	488	532	605	>607	Invitrogen
RH 237	V_m	506	532	687	>710	Invitrogen
Autofluorescence of nicotinamide adenine dinucleotide (NADH)	[NADH]	340	365 ± 5 (filtered Hg lamp)	455	470 ± 20 455 ± 35	21 61
Autofluorescence of flavoprotein (FP)	[FP]	463	450 ± 10 estimated	530	525 ± 25	61
Luminescence of Oxyphor G3	Microvascular $[O_2]$	635	635 ± 10 estimated	810	>695	61
SKC 463	$[K^+]_e$		540 ± 20	575	575 ± 20	Guy Salama, pers. comm.
JPW 6003, 6033, 6067, 5020	V_m	Various	650 ± 20		>720	49, 50
JPW 5034	V_m		650 ± 20		>850	49
PGH	V_m		540 ± 20		>640	64
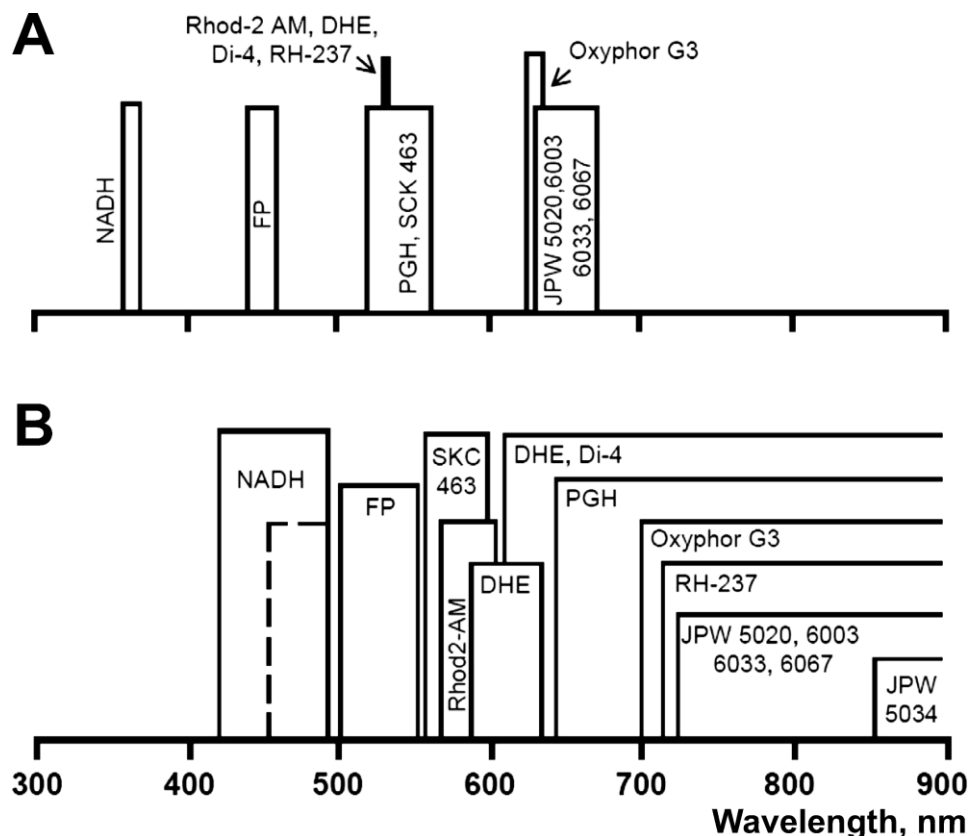
Figure 13. A schematic representation of (A) the excitation and (B) the emission wavelength bands for optical probes that can be used in multimodal cardiac imaging from the data in Table 1. Rhod-2 AM, DHE, Di-4, and RH-237 are all excited by a 532 nm laser line. The width of the rectangles represents the approximate full-width at half maximum of the excitation spectra or the common choices in emission filters. Long-pass filters are open-ended on the right. The heights of the rectangles have no significance other than to aid in data visualization. These data may not always reflect the shift in wavelengths that can occur when the dye is in tissue instead of a solvent.

and spectral deconvolution (60). The use of rapid switching of different illumination wavelengths gated to individual image frames for high-frame-rate, *i.e.*, time-domain multiplexing of multiple metabolic signals, is useful if the excitation spectra do not overlap. The ability of an acousto-optic modulator to control high-speed illumination of the heart has already been demonstrated for older, low-speed CCD cameras (61, 62). An alternative would be to use LEDs of different colors whose pulsed excitation is interleaved and synchronized with the camera frames. Because LEDs have a rise time of microseconds, this approach would be possible as long as each color LED was excited for a sufficiently long train of pulses that it could reach the thermal equilibrium appropriate for the chosen LED duty cycle. The next step will be to apply one of these techniques to multimodal metabolic imaging using modern, high-speed cameras (63) to interleave different metabolic images in a high-speed movie.

The dual imaging of NADH and either $[Ca^{2+}]_i$, V_m, or ROS is particularly appealing, since NADH is an important coenzyme that is critical to the synthesis of ATP and provides a measure of intracellular reduction potential. NADH is a main electron donor for the respiratory chain. Oxidation of NADH is coupled to the phosphorylation of ADP in the production of ATP. Because NADH is autofluorescent, absorbing 320–380 nm and emitting between 420–490 nm, and oxidized NAD^+ is not in these wavelength ranges, it is possible to use fluorescence imaging of NADH as a measure of the metabolic oxidation-reduction state (25). As mitochondrial dysfunction is known to be involved in many diseases, such as Alzheimer's and ischemia, measuring NADH is greatly important. In the ATP-demanding heart, most of the consumed energy is for contraction. Hypoxic and ischemic conditions block the electron transport chain and cause NADH accumulation because oxygen levels are insufficient to continue oxidative phosphorylation. Thus NADH imaging is useful to investigate cardiac ischemia and ischemia/reperfusion (32, 36, 37, 64–66).

Ranji *et al*. (67) used a fiber-optic coupled, rotating-filter, time-interleaved fluorimeter to measure both NADH and flavoprotein (FP) autofluorescence during normal perfusion, regional ischemia (coronary artery ligation), and then reperfusion in the open-chest rabbit heart to assess the myocardial redox ratio, *Redox Ratio = FP/(FP + NADH)*, and hence myocyte apoptosis. In measurements of the isolated rabbit heart, this measurement was supplemented by the measurement of microvascular oxygen with the
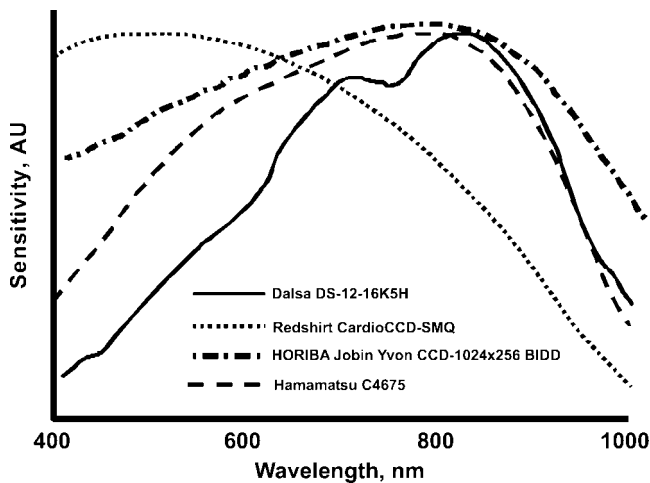
Figure 14. The spectral response of CCD cameras and PDA. The Dalsa DS-12–16K5H (www.dalsa.com) is given in digital number/(nJ/cm2), the Redshirt CardioCCD-SMQ (www.redshirtimaging.com) and HORIBA Jobin Yvon CCD-1024x256 BIDD (www.jobinyvon.com) are given in quantum efficiency, and the Hamamatsu C4675 (www.hamamatsu.com) in photosensitivity A/W. The figure was created using the datasheets found at the URLs shown.

phosphorescent oxygen probe, Oxyphor G3, which was dissolved into the blood plasma (68). Together, these three measurements may provide a measurement of intracellular and intravascular metabolic loads suitable for use in the cardiac operating room. Additionally, the development of new infrared voltage-sensitive dyes may relieve some of the spectral crowding evident in Figure 13 and also allow imaging V_m in blood-perfused hearts and deep into the myocardium (57–59). The excitation and emission wavelengths for these fluorescent indicators are shown in Table 1 and Figure 13.

The measurement of more than one cardiac variable at a time will provide the ability to study the connections between CEP and metabolism. In the dual camera system we have described, simultaneous recording of NADH and V_m was achieved by using two illumination sources (Fig. 1B). In this configuration for concurrent NADH and $[Ca^{2+}]_i$ imaging, if the calcium fluorophore Rhod-2 AM is utilized, only the long pass filter (LPF) needs to be replaced with one having a shorter cutoff wavelength. To accomplish the simultaneous recording of ROS (DHE) and V_m (Rh-237), one light source is sufficient (Table 1, Fig. 13). The possibility of using a second light source for excitation of the new long-wavelength potentiometric dyes (59) in simultaneous measurements of ROS and V_m also exists.

Most CCD cameras are optimized to detect visible light, and their sensitivity falls off rapidly at wavelengths longer than 800 nm. The spectral response of our Dalsa and Redshirt cameras, along with a popular 16×16 Hamamatsu photodiode array (PDA) and a Horiba camera with a near infrared (NIR) optimized deep depletion CCD, are shown in Figure 14. As indicated, the manufacturers use different

units to describe spectral response, but the qualitative performance in the NIR can be inferred from the plots.

The Redshirt and Dalsa cameras have a significant response well into the NIR, although both fall off rapidly. The use of the Redshirt gain feature (3 dB to 30 dB available) was demonstrated in the ratiometric example and could be used to compensate for lower sensitivity when using IR dyes. Dual-rate imaging could also be used with or without gain to make low-noise recordings of a slow metabolic variable in the NIR. For example, the Redshirt can run as slow as 30 frames/sec. The longer integration times at lower frame rates greatly improve SNR. Even when using dual-rate imaging, if both cameras use the same spatial resolution, our calibration method could still be used.

It is important to realize that typically the changes in metabolic variables are slow relative to either V_m or $[Ca^{2+}]_i$. If electromechanical uncouplers are not applied, the fast changes in the metabolic optical signal will signify the motion deflections, and therefore can be used for motion-correction of V_m or $[Ca^{2+}]_i$ from the fluorescence recordings. It has been demonstrated that utilizing the "silent" part of the spectrum insensitive to fast changes in $[Ca^{2+}]_i$ and V_m as the numerator in ratiometry is efficient in reducing motion artifacts in both quantities (31). The rapid change of illumination sources and filters within a motorized filter wheel would allow determination of multiple interleaved images, particularly if they involve different time scales.

In conclusion it should be emphasized that such cardiac disturbances as hyperkalemia, anoxia, and "energy starvation" of the myocardium, all of which can be viewed as metabolic disorders with CEP manifestations, can be produced by (or perhaps be the result of) regional ischemia from coronary artery disease, tachycardia-induced remodeling, or congestive heart failure. The development of metabolic therapies for CEP abnormalities requires simultaneous observation of CEP and metabolism, and a mechanistic understanding of the relationship between the two. Our analysis of the potential for dual camera systems and the simple implementation that we report are our first steps towards advancing our understanding of "electrometabolic" cardiac disorders and their clinical treatment. Our review of related efforts to extend the optical measurements of myocardial function suggests that this is a rich field worthy of expanded research.

1. Gray RA, Iyer A, Bray M-A, Wikswo JP. Voltage-calcium state-space dynamics during initiation of reentry. Heart Rhythm 3:247–248, 2006.

2. Choi BR, Salama G. Simultaneous maps of optical action potentials and calcium transients in guinea-pig hearts: mechanisms underlying concordant alternans. J Physiol 529:171–188, 2000.

3. Laurita KR, Singal A. Mapping action potentials and calcium transients simultaneously from the intact heart. Am J Physiol Heart 280:H2053–H2060, 2001.

4. Efimov IR, Nikolski VP, Salama G. Optical imaging of the heart. Circ Res 95:21–33, 2004.

5. Omichi C, Lamp ST, Lin SF, Yang JZ, Baher A, Zhou SM, *et al*. Intracellular Ca dynamics in ventricular fibrillation. Am J Physiol Heart 286:H1836–H1844, 2004.

6. Hwang GS, Hayashi H, Tang L, Ogawa M, Hernandez H, Tan AY, *et al*. Intracellular calcium and vulnerability to fibrillation and defibrillation in Langendorff-perfused rabbit ventricles. Circulation 114:2595–2603, 2006.

7. Woods MC, Sidorov VY, Holcomb MR, Beaudoin DL, Roth BJ, Wikswo JP. Virtual electrode effects around an artificial heterogeneity during field stimulation of cardiac tissue. Heart Rhythm 3:751–752, 2006.

8. Langrill DM, Roth BJ. The effect of plunge electrodes during electrical stimulation of cardiac tissue. IEEE Trans Biomed Eng 48:1207–1211, 2001.

9. Hoeker GS, Katra RP, Laurita KR. Imaging cellular calcium dysfunction in the heart using multi-modal optical mapping. EMBS: 571–575, 2006.

10. Katra RP, Pruvot E, Laurita KR. Intracellular calcium handling heterogeneities in intact guinea pig hearts. Am J Physiol Heart Circ Physiol 286:H648–H656, 2004.

11. Chuck ET, Meyers K, France D, Creazzo TL, Morley GE. Transitions in ventricular activation revealed by two-dimensional optical mapping. Anat Rec A Discov Mol Cell Evol Biol 280A:990-1000, 2004.

12. Evertson DW, Holcomb MR, Eames M, Bray M, Sidorov VY, Xu J, *et al*. High-resolution high-speed panoramic cardiac imaging system. IEEE Trans Biomed Eng 55:1241–1243, 2008.

13. Bray M-A, Lin S-F, Wikswo JP Jr. Three-dimensional surface reconstruction and fluorescent visualization of cardiac activation. IEEE Trans Biomed Eng 47:1382–1391, 2000.

14. Berger T, Borgdorff A, Crochet S, Neubauer FB, Lefort S, Fauvet B, *et al*. Combined voltage and calcium epifluorescence imaging in vitro and in vivo reveals subthreshold and suprathreshold dynamics of mouse barrel cortex. J Neurophysiol 97:3751–3762, 2007.

15. Zitova B, Flusser J. Image registration methods: a survey. Image Vis Comput 21:977-1000, 2003.

16. Gonzalez RC, Woods RE. Digital Image Processing. Reading: Addison-Wesley, 1993.

17. Bajcsy R, Kovacic S. Multiresolution elastic matching. Comput Vis Graph 46:1–21, 1989.

18. Sidorov VY, Holcomb MR, Woods MC, Gray RA, Wikswo JP. Effects of unipolar stimulation on voltage and calcium distributions in the isolated rabbit heart. Basic Res Cardiol 103:537–551, 2008.

19. Woods MC. Field stimulation of the diastolic rabbit heart: The role of shock strength and duration on epicardial activation and propagation. Vanderbilt University: 2005.

20. Kim YH, Garfinkel A, Ikeda T, Wu TJ, Athill CA, Weiss JN, *et al*. Spatiotemporal complexity of ventricular fibrillation revealed by tissue mass reduction in isolated swine right ventricle. Further evidence for the quasiperiodic route to chaos hypothesis. J Clin Invest 100:2486–2500, 1997.

21. Holcomb MR, Bekele RY, Lima EA, Wikswo JP. Universal serial bus powered and controlled isolated constant-current physiological stimulator. Rev Sci Instrum 79:1261031–1261033, 2008.

22. Mashburn DN, Hinkson SJ, Woods MC, Gilligan JM, Holcomb MR, Wikswo JP. A high-voltage cardiac stimulator for field shocks of a whole heart in a bath. Rev Sci Instrum 78:104302, 2007.

23. Kodama I, Sakuma I, Shibata N, Knisley SB, Niwa R, Honjo H. Regional differences in arrhythmogenic aftereffects of high intensity DC stimulation in the ventricles. Pacing Clin Electrophysiol 23:807–817, 2000.

24. Entcheva E, Kostov Y, Tchernev E, Tung L. Fluorescence imaging of electrical activity in cardiac cells using an all-solid-state system. IEEE Trans Biomed Eng 51:333–341, 2004.

25. Mayevsky A, Rogatsky GG. Mitochondrial function in vivo evaluated by NADH fluorescence: from animal models to human studies. Am J Physiol Cell 292:C615–C640, 2007.

26. Bray M-A, Aliev RR, Wikswo JP Jr. Use of topological charge to determine filament location in a numerical model of scroll wave activity. IEEE Trans Biomed Eng 49:1086–1093, 2002.

27. Al Khadra A, Nikolski V, Efimov IR. The role of electroporation in defibrillation. Circ Res 87:797–804, 2000.

28. Brandes R, Figueredo VM, Camacho SA, Massie BM, Weiner MW. Suppression of motion artifacts in fluorescence spectroscopy of perfused hearts. Am J Physiol 263:H972–H980, 1992.

29. Kong W, Johnson PL, Knisley SB. Reduction of motion artifacts and photobleaching during multiwavelength ratiometric optical recording of action potentials and intracellular calcium transients in rabbit hearts. Pacing Clin Electrophysiol 23:608, 2000.

30. Knisley SB, Justice RK, Kong W, Johnson PL. Ratiometry of transmembrane voltage-sensitive fluorescent dye emission in hearts. Am J Physiol Heart 279:H1421–H1433, 2000.

31. Kong W, Walcott GP, Smith WM, Johnson PL, Knisley SB. Emission ratiometry for simultaneous calcium and action potential measurements with coloaded dyes in rabbit hearts: reduction of motion and drift. J Cardiovasc Electrophysiol 14:76–82, 2003.

32. Stoner JD, Angelos MG, Clanton TL. Myocardial contractile function during postischemic low-flow reperfusion: critical thresholds of NADH and O-2 delivery. Am J Physiol Heart 286:H375–H380, 2004.

33. Brandes R, Bers DM. Simultaneous measurements of mitochondrial NADH and Ca2+ during increased work in intact rat heart trabeculae. Biophys J 83:587–604, 2002.

34. Salama G, Lombardi R, Elson J. Maps of optical action-potentials and NADH fluorescence in intact working hearts. Am J Physiol 252:H384–H394, 1987.

35. Fjeld CC, Birdsong WT, Goodman RH. Differential binding of NAD+ and NADH allows the transcriptional corepressor carboxyl-terminal binding protein to serve as a metabolic sensor. Proc Natl Acad Sci U S A 100:9202–9207, 2003.

36. Kevin LG, Camara AKS, Riess ML, Novalija E, Stowe DF. Ischemic preconditioning alters real-time measure of O-2 radicals in intact hearts with ischemia and reperfusion. Am J Physiol Heart 284:H566–H574, 2003.

37. Lu LS, Liu YB, Sun CW, Lin LC, Su MJ, Wu CC. Optical mapping of myocardial reactive oxygen species production throughout the reperfusion of global ischemia. J Biomed Opt 11:021012, 2006.

38. Myerburg RJ, Kessler KM, Castellanos A. Sudden cardiac death—structure, function, and time-dependence of risk. Circulation 85:2–10, 1992.

39. Katz AM. Heart Failure: Pathophysiology, molecular biology, and clinical management. Philadelphia: Lippincott Williams & Wilkins, 2000.

40. Lane RE, Cowie MR, Chow AWC. Prediction and prevention of sudden cardiac death in heart failure. Heart 91:674–680, 2005.

41. Roden DM. CAST: implications for the use of antiarrhythmic agents in the setting of ischemic heart disease. Coron Artery Dis 2:723–729, 1991.

42. Greene HL, Roden DM, Katz RJ, Woosley RL, Salerno DM, Henthorn RW. The Cardiac-Arrhythmia Suppression Trial: first CAST...then CAST-II. J Am Coll Cardiol 19:894–898, 1992.

43. Prystowsky EN, Freeland S, Branyas NA, Rardon DP, Fogel RI, Padanilam BJ, *et al*. Clinical experience with dofetilide in the treatment of patients with atrial fibrillation. J Cardiovasc Electrophysiol 14:S287–S290, 2003.

44. Brendorp B, Pedersen OD, Torp-Pedersen C, Sahebzadah N, Kober L. A benefit-risk assessment of class III antiarrhythmic agents. Drug Saf 25:847–865, 2002.

45. Myerburg RJ, Mitrani R, Interian A, Castellanos A. Interpretation of

outcomes of antiarrhythmic clinical trials—design features and population impact. Circulation 97:1514–1521, 1998.

46. Shah M, Akar FG, Tomaselli GF. Molecular basis of arrhythmias. Circulation 112:2517–2529, 2005.

47. Moss AJ, Hall J, Cannom DS, Daubert JP, Higgins SL, Klein H, *et al.* Improved survival with an implanted defibrillator in patients with coronary disease at high risk for ventricular arrhythmia. N Engl J Med 335:1933–1940, 1996.

48. Bardy GH, Lee KL, Mark DB, Poole JE, Packer DL, Boineau R, *et al.* Amiodarone or an implantable cardioverter-defibrillator for congestive heart failure. N Engl J Med 352:225–237, 2005.

49. Buxton AE, Lee KL, DiCarlo L, Echt DS, Fisher JD, Greer S, *et al.* Nonsustained ventricular tachycardia in coronary artery disease: relation to inducible sustained ventricular tachycardia. Ann Intern Med 125:35–39, 1996.

50. Connolly SJ, Gent M, Roberts RS, Dorian P, Roy D, Sheldon RS, *et al.* Canadian implantable defibrillator study (CIDS)—a randomized trial of the implantable cardioverter defibrillator against amiodarone. Circulation 101:1297–1302, 2000.

51. Moss AJ, Zareba W, Hall WJ, Klein H, Wilber DJ, Cannom DS, *et al.* Prophylactic implantation of a defibrillator in patients with myocardial infarction and reduced ejection fraction. N Engl J Med 346:877–883, 2002.

52. McAnulty J, Halperin B, Kron J, Larsen G, Raitt M, Swenson R, *et al.* A comparison of antiarrhythmic-drug therapy with implantable defibrillators in patients resuscitated from near-fatal ventricular arrhythmias. N Engl J Med 337:1576–1583, 1997.

53. Ellinor PT, Milan DJ, MacRae CA. Metabolic gene defects and risk of arrhythmia. Heart and Metabolism 33:9–12, 2006.

54. Taegtmeyer H. Cardiac metabolism as a target for the treatment of heart failure. Circulation 110:894–896, 2004.

55. Brame CJ, Boutaud O, Davies SS, Yang T, Oates JA, Roden D, *et al.* Modification of proteins by isoketal-containing oxidized phospholipids. J Biol Chem 279:13447–13451, 2004.

56. Fukuda K, Davies SS, Nakajima T, Ong BH, Kupershmidt S, Fessel J, *et al.* Oxidative mediated lipid peroxidation recapitulates proarrhythmic effects on cardiac sodium channels. Circ Res 97:1262–1269, 2005.

57. Matiukas A, Mitrea BG, Pertsov AM, Wuskell JP, Wei MD, Watras J, *et al.* New near-infrared optical probes of cardiac electrical activity. Am J Physiol Heart 290:H2633–H2643, 2006.

58. Matiukas A, Mitrea BG, Qin M, Pertsov AM, Shvedko AG, Warren MD, *et al.* Near-infrared voltage-sensitive fluorescent dyes optimized for optical mapping in blood-perfused myocardium. Heart Rhythm 4: 1441–1451, 2007.

59. Salama G, Choi BR, Azour G, Lavasani M, Tumbev V, Salzberg BM, *et al.* Properties of new, long-wavelength, voltage-sensitive dyes in the heart. J Membr Biol 208:125–140, 2005.

60. Zimmermann T, Rietdorf J, Pepperkok R. Spectral imaging and its applications in live cell microscopy. FEBS Lett 546:87–92, 2003.

61. Wikswo JP Jr, Lin S-F, Abbas RA. Virtual electrodes in cardiac tissue: a common mechanism for anodal and cathodal stimulation. Biophys J 69:2195–2210, 1995.

62. Lin SF, Abbas RA, Wikswo JP. High-resolution high-speed synchronous epifluorescence imaging of cardiac activation. Rev Sci Instrum 68: 213–217, 1997.

63. Choi BR, Jang W, Salama G. Spatially discordant voltage alternans cause wavebreaks in ventricular fibrillation. Heart Rhythm 4:1057–1068, 2007.

64. Riess ML, Camara AKS, Chen Q, Novalija E, Rhodes SS, Stowe DF. Altered NADH and improved function by anesthetic and ischemic preconditioning in guinea pig intact hearts. Am J Physiol Heart Circ Physiol 283:H53–H60, 2002.

65. Akar FG, Aon MA, Tomaselli GF, O'Rourke B. The mitochondrial origin of postischemic arrhythmias. J Clin Invest 115:3527–3535, 2005.

66. Zhu X, Zuo L, Cardounel AJ, Zweier JL, He G. Characterization of in vivo tissue redox status, oxygenation, and formation of reactive oxygen species in postischemic myocardium. Antioxid Redox Signal 9:447–455, 2007.

67. Ranji M, Kanemoto S, Matsubara M, Grosso MA, Gorman JH, Gorman RC, *et al.* Fluorescence spectroscopy and imaging of myocardial apoptosis. J Biomed Opt 11:0640361–0640364, 2006.

68. Ranji M, Jaggard DL, Apreleva SV, Vinogradov SA, Chance B. Simultaneous fluorometry and phosphorometry of Langendorff perfused rat heart: ex vivo animal studies. Opt Lett 31:2995–2997, 2006.

ERRATUM

In the article entitled "The Potential of Dual Camera Systems for Multimodal Imaging of Cardiac Electrophysiology and Metabolism" by Mark R. Holcomb, Marcella C. Woods, Ilija Uzelac, John P. Wikswo, Jonathan M. Gilligan, and Veniamin Y. Sidorov, which was published in Experimental Biology and Medicine 234:1355–1373, 2009, there was a typographical error on page 1360 in the link to the C source code to dual camera alignment. The correct link is www.vanderbilt.edu/viibre/technologies.html. The authors regret this oversight.